Numerical Heat Transfer, Part A, 49: 369–391, 2006
Copyright © Taylor & Francis Group, LLC
ISSN: 1040-7782 print/1521-0634 online
DOI: 10.1080/10407780500359901

Taylor & Francis
Taylor & Francis Group

NUMERICAL ANALYSIS OF RADIATIVE EFFECTS ON NATURAL CONVECTION IN VERTICAL CONVERGENT AND SYMMETRICALLY HEATED CHANNELS

Nicola Bianco
Dipartimento di Energetica, Termofluidodinamica applicata e Condizionamenti ambientali, Università degli Studi di Napoli Federico II, Piazzale Tecchio, Napoli, Italy

Luigi Langellotto and Oronzio Manca
Dipartimento di Ingegneria Aerospaziale e Meccanica, Seconda Università degli Studi di Napoli, Aversa (CE), Italy

Vincenzo Naso
Dipartimento di Energetica, Termofluidodinamica applicata e Condizionamenti ambientali, Università degli Studi di Napoli Federico II, Piazzale Tecchio, Napoli, Italy

Natural convection in a convergent channel with finite-thickness principal walls at uniform heat flux is investigated numerically. Heat conduction in the walls and the effects of walls emissivity are taken into account. Laminar two-dimensional steady-state conditions are assumed. Results in terms of wall dimensionless temperature profiles as a function of convergence angle, channel spacing, and heat flux are given for various values of wall emissivity. Wall temperatures decrease significantly, passing from $\delta = 0^\circ$ to 2° at the lowest channel spacing. Streamlines and temperature fields show a recirculating region in the channel for large values of L_w/b_{min} and for δ equal to 5° and 10°. Correlations between Nusselt numbers and Rayleigh numbers are proposed. Dimensionless parameters are in the following ranges: $4.4 \le Ra'_{bmin} \le 1.5 \times 10^5$, $10 \le L_w/b_{min} \le 58$, $0.0 \le \varepsilon \le 1.0$, and $0^\circ \le \delta \le 10^\circ$. Numerical predictions are in very good agreement with experimental data.

INTRODUCTION

Thermal design of natural-convection systems often requires an accurate prediction of the performance of geometric configurations [1, 2]. The optimization of simple configurations and the design of configurations derived from simple channels [3–5] are recent trends in air natural convection between plates for electronic cooling.

Received 18 November 2004; accepted 8 August 2005.

This work was supported by Ministero dell'Istruzione, dell'Università e della Ricerca with a 2003–2005 Progetto di Ricerca d'Interesse Nazionale grant and Seconda Università degli Studi di Napoli with 2003 and 2005 research grants.

Address correspondence to Oronzio Manca, Dipartimento di Ingegneria Aerospaziale e Meccanica, Seconda Università degli studi di Napoli, Via Roma, 29-81031, Aversa (CE), Italy. E-mail: oronzio.manca@unina2.it

NOMENCLATURE

a	thermal diffusivity, m^2/s
b	channel spacing, m
g	acceleration of gravity, m/s^2
Gr	Grashof number, Eq. (9)
I	radiation intensity, W/m^2
k	thermal conductivity, W/m K
L	channel length, m
L_x, L_y	reservoir dimensions, m
n	normal to the wall
N_R	radiation to conduction parameter, Eq. (12)
Nu_b	convective Nusselt number, Eq. (10)
Nu_b^*	convective and radiative Nusselt number, Eq. (10)
p	pressure, Pa
Pr	Prandtl number
q	heat flux, W/m^2
r^2	regression coefficient
Ra'_b	convective Rayleigh number, Eq. (9)
Ra'^*_b	convective and radiative Rayleigh number, Eq. (9)
s	ray direction vector
t	wall thickness, m
T	temperature, K
u	velocity component along x axis, m/s
v	velocity component along y axis, m/s
x, y	coordinates along the plate, m
β	volumetric coefficient of expansion, 1/K
δ	half-angle from the vertical, $^\circ$
ε	wall emissivity
θ	dimensionless temperature, Eq. (6)
ν	kinematic viscosity, m^2/s
ρ	density, kg/m^3
σ	Stefan-Boltzmann constant, $W/m^2\ K^4$
Ω	hemispherical solid angle, sr
ψ	stream function, m^2/s
Ψ	dimensionless stream function

Subscripts

av	average
c	convective
f	fluid
in	incident
max	maximum
min	minimum
o	ambient air
r	radiative
s	solid
w	wall
x	refers to the x coordinate

Heat transfer in a convergent channel with two uniformly heated flat plates is an interesting problem. Evaluating the thermal performance of these configurations is rather difficult, because of the large number of thermal and geometric variables. Therefore, experimental and numerical investigations can give useful information on the effects of the heat flux, the inclination angle, and the spacing.

The first numerical and experimental study on natural convection in water in a convergent vertical channel was carried out by Sparrow et al. [6]. The principal converging walls were maintained at the same uniform temperature. The angles from the vertical varied between 0° and 15° and the modified Rayleigh number, based on the maximum channel spacing, was in the 10^4–10^8 range. By employing correlation variables based on the maximum interwall spacing as the characteristic dimension, the authors found that Nusselt numbers for the convergent channels were in good agreement with those for the parallel-walled channel. Natural convection in air in uniform wall temperature converging channels was investigated experimentally using a speckle-gram technique in [7]. Local and average heat transfer coefficients were evaluated for five inclination angles and eight channel exit openings. Correlations for both local and average Nusselt numbers were derived. The characteristics of the thermal layers were visualized using a Schlieren technique. Natural convection in air in a convergent vertical channel with uniform wall temperature was investigated numerically in [8]. The best correlation for Nusselt number at low Rayleigh numbers ($<10^2$) was obtained by assuming the maximum channel spacing as the characteristic dimension.

The same configuration was studied numerically and experimentally in [9], where the computational domain was extended upstream and downstream of the channel. The experimental investigation was carried out using the Mach-Zender interferometer. It was observed that at low Rayleigh numbers, the larger the inclination angle the larger the Nusselt number, whereas the opposite occurred at high Rayleigh numbers. A numerical analysis on natural convection in converging channels for various angles of convergence was presented in [10]. Comparisons between numerical and experimental results from the literature were carried out as well. Recently, a numerical simulation and optimization for laminar natural convection in vertical diverging and converging channels was reported in [11]. The study was carried out for nonuniform wall heating, which was modeled as an isothermal zone with its length less than or equal to the wall length. The adiabatic region was located either at the bottom end or at the top end of the channel. Numerical simulations were carried out using the commercial code FIDAP and were obtained for Rayleigh numbers, based on the wall length, in the 10^5–10^6 range. For converging channels, results showed that the optimal angle between the two walls was approximately zero at large Rayleigh numbers.

An experimental investigation on natural convection in air in a convergent channel, uniformly heated at the principal walls, was carried out in [12], in order to analyze the effects of radiative heat transfer. Flow visualization showed the existence of a recirculating region in the upper part of the channel for small values of the minimum channel spacing and for convergence angles equal to 5° and 10°. It was found that maximum temperature differences between temperature profiles at $\varepsilon = 0.10$ and 0.90 were attained for the largest convergence angle, the maximum channel spacing, and the larger wall heat flux. Correlations for dimensionless maximum wall temperatures and average Nusselt numbers in terms of channel Rayleigh numbers were proposed. The best correlations were obtained for Rayleigh numbers referred to the maximum channel spacing. The same configuration, without radiative effects, was investigated numerically in [13], where the computational domain was extended upstream and downstream of the channel. The two principal flat plates, at uniform heat flux, were considered to have finite thickness and to be thermally conductive. When the larger value of the walls' thermal conductivity was used in the numerical model, numerical predictions were in line with experimental data, except in the exit region of the channel, since the numerical model did not take into account radiative and conductive end effects.

Thermal radiation is significant in natural convection, in both partially open-ended cavities and closed cavities, as was shown in [14]. Nevertheless, few articles deal with the effect of thermal radiation, particularly for symmetric heating. A first numerical study on the interaction of radiation with developing laminar natural convection in an asymmetrically heated channel was carried out in [15]. Results showed that for black surfaces the maximum wall temperature was half that attained in the case with no radiation. Results presented in [16] showed that the effect of the walls emissivity was more significant in an asymmetrically heated channel. Natural convection and radiation cooling in a vented channel was analyzed numerically in [17]. It was found that, for a continuously heated channel, vents lessened the overall cooling process. No information was given about the radiative effect. A numerical analysis for thermal management of a tape ball grid array (TBGA) package was carried out in [18]. The package was attached to a card and placed vertically in an adiabatic channel. A conjugate heat transfer model was used, to account for

conduction and radiation in the package and in the card and for mixed convection in the air. Radiation effects turned out to be significant in the natural-convection regime, and as much as 50% of the heat transfer could be accounted for by radiation.

Convergent channels can exhibit a rather large view factor toward the surroundings, which depends on the aperture angle. As a consequence, radiative effects can improve the air natural-convection thermal performance of convergent channels, though symmetrically heated. However, it seems that no information is available about conjugate natural convection in air with radiative heat transfer and conduction in the heated walls of the channel. This is also pointed out in Table 1, where the significant parameters for convergent channels are summarized.

In this article, reference is made to natural convection in air in a convergent channel with finite-thickness principal walls at uniform heat flux. Heat conduction in the walls and the effects of wall emissivity are taken into account. A numerical analysis is carried out in laminar, two-dimensional steady-state conditions. The computational domain has two external reservoirs in order to simulate the momentum and energy diffusions that occur outside the channel, as suggested in [9, 19]. Results in terms of dimensionless wall temperature, stream function, and temperature fields are given. Nusselt numbers are evaluated and simple monomial correlations are proposed in terms of Rayleigh numbers in the ranges $5.0 \leq \mathrm{Ra}^{l*}_{b\min} \leq 2.3 \times 10^5$, $10 \leq L_w/b_{\min} \leq 58$, $0.0 \leq \varepsilon \leq 1.0$, and $0^\circ \leq \delta \leq 10^\circ$. Pictures of flow visualization are also taken and comparisons with numerical results are accomplished. Numerical predictions are compared with experimental data.

MATHEMATICAL DESCRIPTION AND GOVERNING EQUATIONS

The physical domain under investigation is shown in Figure 1*a*. It consists of two nonparallel plates that form a vertical convergent channel. Both plates are thermally conductive, gray, and heated at uniform heat flux. The imbalance between the temperature of the ambient air and the temperature of the heated plates draws an air flow into the channel. The flow in the channel is assumed to be steady-state, two-dimensional, laminar, incompressible, with negligible viscous dissipation. All thermophysical properties of the fluid are assumed to be constant, except for the dependence of the density on the temperature (Boussinesq approximation), which gives rise to buoyancy forces. The thermophysical properties of the air are evaluated at the ambient temperature, T_o, which is assumed to be 300 K in all cases. The ambient is assumed to be a black body at the temperature of 300 K.

With the above assumptions, the governing equations in primitive variables are [20]

$$\frac{\partial u}{\partial x} + \frac{\partial v}{\partial y} = 0 \tag{1}$$

$$u\frac{\partial u}{\partial x} + v\frac{\partial u}{\partial y} = -\frac{1}{\rho_f}\frac{\partial p}{\partial x} + \nu\left(\frac{\partial^2 u}{\partial x^2} + \frac{\partial^2 u}{\partial y^2}\right) \tag{2}$$

$$u\frac{\partial v}{\partial x} + v\frac{\partial v}{\partial y} = -\frac{1}{\rho_f}\frac{\partial p}{\partial y} + \nu\left(\frac{\partial^2 v}{\partial x^2} + \frac{\partial^2 v}{\partial y^2}\right) - g\beta(T - T_o) \tag{3}$$

Table 1. Numerical and experimental studies on natural convection in convergent channels

Reference	Type of investigation	Boundary conditions on channel walls	Conductive walls	Radiative effect	δ	Reference length	L/b	Ra′	Correlation
Sparrow et al. (1988) [6]	Numerical and experimental	UWT	None	None	0°, 2°, 5°, 10°, 15°	b_{max}	11.4, 22.9	$4 \times 10^3 - 7 \times 10^4$	Yes
Kihm et al. (1993) [7]	Numerical and experimental	UWT	None	None	0°, 15°, 30°, 45°, 60°	b_{min}	2.5–14	$1–1 \times 10^8$	None
Said (1996) [6]	Numerical and experimental	UWT	None	None	0°, 2°, 5°, 10°	b_{max}	—	$1–2 \times 10^4$	None
Shalash et al. (1997) [9]	Numerical and experimental	UWT	None	None	0°, 2°, 4°, 8°	$b_{min}/2$	6, 8.5, 12	$6.4–4.8 \times 10^4$	Yes
Kaiser et al. (2004) [10]	Numerical	UWT	None	None	0° to 60°	b_{min}	0.5–50	$1–1 \times 16^6$	Yes
Bejan et al. (2004) [11]	Numerical	UWT	None	None	0° to 5°	L_w	—	$1 \times 10^5–1 \times 10^7$	None
Bianco et al. (2003) [12]	Experimental	UWHF	Yes	Yes	0°, 2°, 5°, 10°	b_{max}	10–58	$4.4–2.9 \times 10^8$	Yes
Bianco and Nardini (2004) [13]	Numerical	UWHF	Yes	None	0°, 2°, 5°, 10°	b_{max}	10–58	$4.4–2.9 \times 10^8$	Yes
Present work	Numerical and experimental	UWHF	Yes	Yes	2°, 10°	b_{max}	10–58	$4.4–2.9 \times 10^8$	Yes

UWT: Uniform Wall Temperature.
UWHF: Uniform Wall Heat Flux.

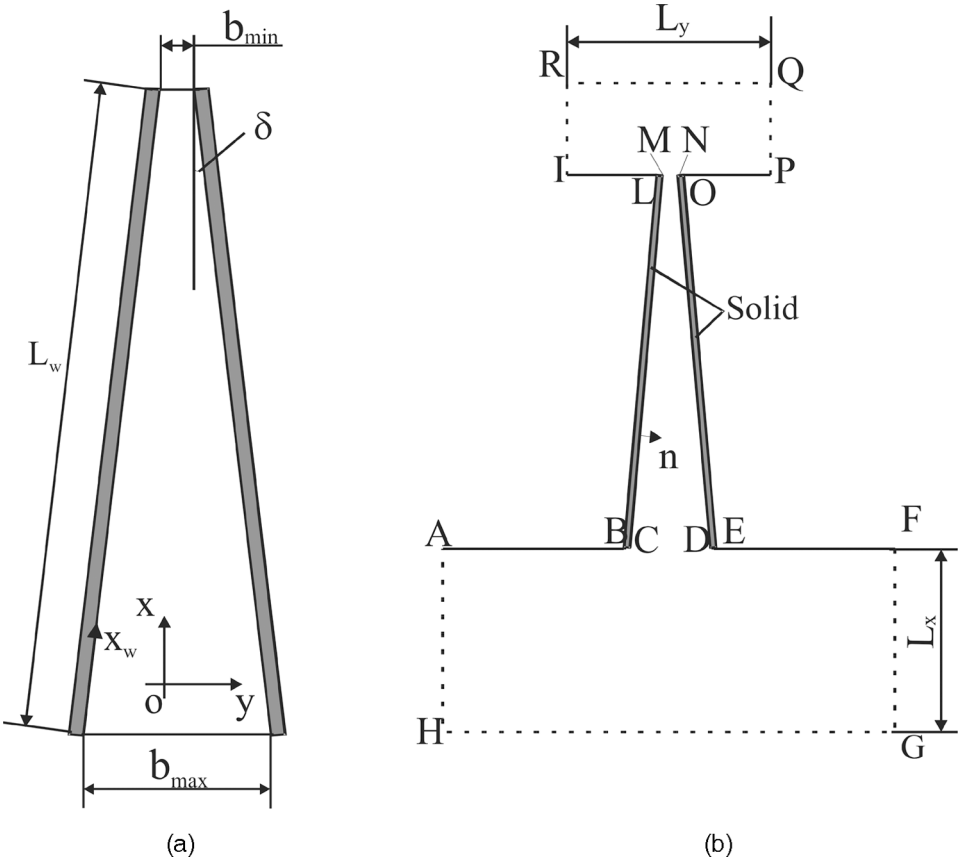

Figure 1. Sketch of the configuration: (*a*) physical domain; (*b*) computational domain.

$$u\frac{\partial T}{\partial x}+v\frac{\partial T}{\partial y}=a_f\left(\frac{\partial^2 T}{\partial x^2}+\frac{\partial^2 T}{\partial y^2}\right) \tag{4}$$

A two-dimensional conduction model is employed. The heat conduction equation in the plates at steady-state conditions, with constant thermophysical properties, is

$$\frac{\partial^2 T_s}{\partial x^2}+\frac{\partial^2 T_s}{\partial y^2}=0 \tag{5}$$

Reference to dimensionless quantities is made in the following. A dimensionless wall temperature can be defined as

$$\theta_w^*=\frac{(T-T_o)k}{(q_c+q_r)b_{\min}} \tag{6}$$

The term $(q_c + q_r)$ is considered in order to account for the global heat transfer from the channel plates, both convective to the fluid, q_c, and radiative to the ambient, q_r. The term $(q_c + q_r)$ is not equal to the heat rate supplied to the walls, q_w, since the model takes into account heat losses to the ambient because of the edge effects from the upper and lower sides of the plates.

The terms q_c and q_r are evaluated by the following relations:

$$q_c = \frac{1}{L_w}\int_0^{L_w} q_{c,x}(x)\,dx \qquad q_r = \frac{1}{L_w}\int_0^{L_w} q_{r,x}(x)\,dx \tag{7}$$

The stream function is

$$\frac{\partial \psi}{\partial y} = u \qquad \frac{\partial \psi}{\partial x} = -v \tag{8}$$

and its dimensionless value is $\Psi = \psi/v$.

Two Rayleigh numbers and two average Nusselt numbers are considered:

$$\mathrm{Ra}'_b = \mathrm{Gr}_b\ \mathrm{Pr} = \frac{g\beta\, q_c b^5}{\nu^2 k_f L}\mathrm{Pr} \qquad \mathrm{Ra}'^{*}_b = \mathrm{Gr}^{*}_b\ \mathrm{Pr} = \frac{g\beta\,(q_c + q_r) b^5}{\nu^2 k_f L}\mathrm{Pr} \tag{9}$$

$$\mathrm{Nu}_b = \frac{q_c b}{(T_{w,\mathrm{av}} - T_o)k_f} \qquad \mathrm{Nu}^{*}_b = \frac{(q_c + q_r)b}{(T_{w,\mathrm{av}} - T_o)k_f} \tag{10}$$

where b is $b_{\min}$, b_{av}, or $b_{\max}$ and the average wall temperature is

$$T_{w,\mathrm{av}} = \frac{1}{L_w}\int_0^{L_w} T_w(x)\,dx \tag{11}$$

The conjugate conductive-convective-radiative heat transfer is properly accounted for by the dimensionless parameter [21]

$$N_R = \frac{\sigma T_o^3 b_{\min}}{k_f} \tag{12}$$

NUMERICAL PROCEDURE

Since the two plates are placed in an infinite medium, from a numerical point of view the problem is solved with reference to a computational domain of finite extension, as depicted in Figure 1*b*, and by following the approach given in [9, 13, 19]. This computational domain allows us to account for the diffusive effects peculiar to the elliptic model. They occur outside of the channel, both upstream and downstream, and can significantly affect the thermal and fluidynamic patterns. Furthermore, a finite-extension computational domain has been employed in this investigation in order to simulate the free-stream condition of the flow far away from the region of the thermal disturbance induced by the heated plates.

Table 2. Boundary conditions for the fluid domain

Wall	u	v	T
AH and FG	$\frac{\partial u}{\partial y}=0$	$\frac{\partial v}{\partial y}=0$	$T=T_o$
HG	$\frac{\partial u}{\partial x}=0$	$\frac{\partial v}{\partial x}=0$	$T=T_o$
AB, EF, IL, OP	$u=0$	$v=0$	$\frac{\partial T}{\partial x}=0$
BC, DE, LM, NO	$u=0$	$v=0$	$k_f\frac{\partial T}{\partial x}=k_s\frac{\partial T}{\partial x}$
DN	$u=0$	$v=0$	$k_f\frac{\partial T}{\partial n}=k_s\frac{\partial T}{\partial n}+q_w+q_r$
CM	$u=0$	$v=0$	$k_f\frac{\partial T}{\partial n}=k_s\frac{\partial T}{\partial n}-q_w+q_r$
RQ	$\frac{\partial u}{\partial x}=0$	$\frac{\partial v}{\partial x}=0$	$\begin{cases}\frac{\partial T}{\partial x}=0 & \text{if } u>0\\ T=T_o & \text{if } u<0\end{cases}$
IR	$\frac{\partial u}{\partial y}=0$	$\frac{\partial v}{\partial y}=0$	$\begin{cases}\frac{\partial T}{\partial y}=0 & \text{if } v>0\\ T=T_o & \text{if } v<0\end{cases}$
QP	$\frac{\partial u}{\partial y}=0$	$\frac{\partial v}{\partial y}=0$	$\begin{cases}\frac{\partial T}{\partial y}=0 & \text{if } v>0\\ T=T_o & \text{if } v<0\end{cases}$

The imposed boundary conditions are reported in Table 2 for the fluid domain and in Table 3 for the solid domain. The pressure defect equals zero on the inlet and outlet boundaries. The net radiative heat flux from the surface is then computed as the sum of the reflected fraction of the incident and emitted heat fluxes:

$$q_r(x)=(1-\varepsilon)q_{\text{in}}(x)+\varepsilon\,\sigma\,T_w^4(x) \tag{13a}$$

$$q_{\text{in}}(x)=\int_{s\cdot n>0} I_{\text{in}}s\cdot n\,d\Omega \tag{13b}$$

The segregated solution method was chosen to solve the governing equations, which were linearized implicitly with respect to dependent variables of the equation.

Table 3. Boundary conditions for the solid domain

Wall	T	ε
DN	$k_f\frac{\partial T}{\partial n}=k_s\frac{\partial T}{\partial n}+q_w+q_r;\ T_w=T_f$	0.00–1.00
CM	$k_f\frac{\partial T}{\partial n}=k_s\frac{\partial T}{\partial n}-q_w+q_r;\ T_w=T_f$	0.00–1.00
BL, OE	$\frac{\partial T}{\partial n}=0$	0.00–1.00
BC, DE, LM, NO	$k_f\frac{\partial T}{\partial x}=k_s\frac{\partial T}{\partial x}+q_r;\ T_w=T_f$	0.00–1.00

The second-order upwind scheme was chosen for unsteady energy and momentum equations [22]. The Semi-Implicit Method for Pressure-Linked Equations (SIMPLE) scheme was chosen to couple pressure and velocity. Similar considerations were made for the choice of the discrete transfer radiation model (DTRM), assuming all surfaces to be diffuse [22, 23]. This means that the reflection of incident radiation at the surface is isotropic with respect to the solid angle. Therefore, the scattering effect is not taken into account. The main assumption of the DTRM is that the radiation leaving a surface element, in a certain range of solid angles, can be approximated by a single ray. Moreover, all the walls are assumed to be gray.

Computation starts with zero values of the velocity components and with pressure and temperature values equal to the ambient ones. The convergence criteria of 10^{-6} for the residuals of the velocity components and of 10^{-8} for the residuals of the energy were assumed.

According to [9, 19], $L_x = L_w$ and $L_y = 10b_{\min}$ were chosen as the reservoir sizes, since the variations in the velocity and the temperature in the channel were small for a larger size of the reservoir.

Preliminary results were obtained to evaluate the effect of the grid. The configuration with $L_w/b_{\min} = 40.6$, $\delta = 10^\circ$ at $\mathrm{Ra}'^{*}_{b\,\min} = 30.0$ and 220 was examined. The dimensionless mass flow rate, obtained as the difference between the stream-function values on the two walls, and the average Nusselt number were evaluated for four different grids, with the following number of nodes in the channel: 50×100, 100×200, 150×300, and 200×400. Differences between numerical results and the asymptotic value, which was obtained with the Richardson extrapolation [24], are reported in Table 4. In the following, numerical simulations are carried out using a grid of 200×400 nodes.

In order to estimate the effect of the discretization on the contribution of radiative heat transfer, the configuration with $\mathrm{Ra}'^{*}_{b\min} = 3.1 \times 10^4$ and 2.25×10^5 and with 3×3, 6×6, 9×9, and 12×12 subdivisions of polar and azimuthal angles, respectively, was considered. Differences between numerical results and the asymptotic value, which was obtained with the aforementioned Richardson extrapolation, are presented in Table 5. One can notice that differences between Nusselt numbers

Table 4. Analysis of grid independence

$\mathrm{Ra}'^{*}_{b\,\min}$	Mesh	$\mathrm{Nu}_{b\min}$	$\Delta\%$	$\Delta\Psi$	$\Delta\%$
30.0	50×100	1.127	1.476	0.005248	0.2882
	100×200	1.112	0.1607	0.005248	0.2882
	150×300	1.115	0.4041	0.005248	0.2882
	200×400	1.111	0.04016	0.005237	0.07391
	Asymptotic value		1.110	0.005233	
220	50×100	1.831	6.8262	0.008965	2.072
	100×200	1.722	0.4667	0.008810	0.3074
	150×300	1.729	0.8751	0.008810	0.3074
	200×400	1.716	0.1167	0.008790	0.07970
	Asymptotic value		1.714	0.008783	

Table 5. Analysis of ray discretization

$Ra^{l*}_{b\,min}$	Divisions of polar and azimuthal angles	$Nu_{b\,min}$	$\Delta\%$	$\Delta\Psi$	$\Delta\%$
3.07×10^4	3×3	5.047	−9.282	0.006395	6.772×10^{-2}
	6×6	4.605	0.2887	0.006398	2.084×10^{-2}
	9×9	4.616	0.05052	0.006397	3.646×10^{-2}
	12×12	4.615	0.07218	0.006399	5.209×10^{-3}
	Asymptotic value	4.618		0.006399	
2.25×10^5	3×3	6.873	1.711	0.01070	0
	6×6	6.982	0.1525	0.01070	0
	9×9	6.995	–0.03337	0.01070	0
	12×12	6.990	0.03813	0.01070	0
	Asymptotic value	6.993		0.01070	

for the 6×6 and 12×12 subdivisions are less than 0.2%. Therefore the 6×6 division has been employed in the following.

EXPERIMENTAL APPARATUS

A sketch of the test section investigated is shown in Figure 2*a*, where x_w and y are the coordinates along the length and the spacing of the channel, respectively. In the experimental tests the channel was made of two vetronite principal plates, heated symmetrically over their entire surfaces with a uniform heat flux, and two unheated Plexiglas side walls. It was open to the ambient along the top and the bottom edges.

Experiments were carried out for emissivity value of the principal walls equal to 0.90. The emissivity value of the walls was obtained by spraying a black varnish onto the wall surface. The radiometric direct measurement of the total normal emissivity was carried out by comparison with a black body with an accuracy of $\pm 5\%$.

Two 4.0-mm-thick trapezoidal Plexiglas plates, placed between the principal walls at their lateral edges, were the side walls of the channel. They were machined within an accuracy of ± 0.03 mm. The distance between the principal walls was measured with an accuracy of ± 0.25 mm by means of a dial-gauge caliper. The inclination angle was set up and verified by measuring the maximum and the minimum spacings. The walls were fastened together with a steel frame, which was designed in such a way as not to obstruct the fluid flow near the channel inlet. A hinge was placed at the top of the principal walls, allowing their rotational movement to obtain a convergent channel. The channel was aligned vertically, with horizontal leading edges, by means of a plumb line and a level.

The principal walls of the channel were 406 mm long and 450 mm wide. The minimum channel gap, b_{min}, was in the range 7.0–40.0 mm. The convergence angle, δ, between the vertical and each inclined plate varied in the 0°–10° range. Wall temperature measurements were carried out by 0.50-mm-OD iron–constantan (type J) thermocouples, embedded in the fiberboard very close to the back side of the copper layer and bound with a 3 M epoxy glue. Twenty-three thermocouples were placed in the centerline of each plate. The ambient air temperature was measured by the same type of thermocouples located near the leading edge of the channel. Thermocouple

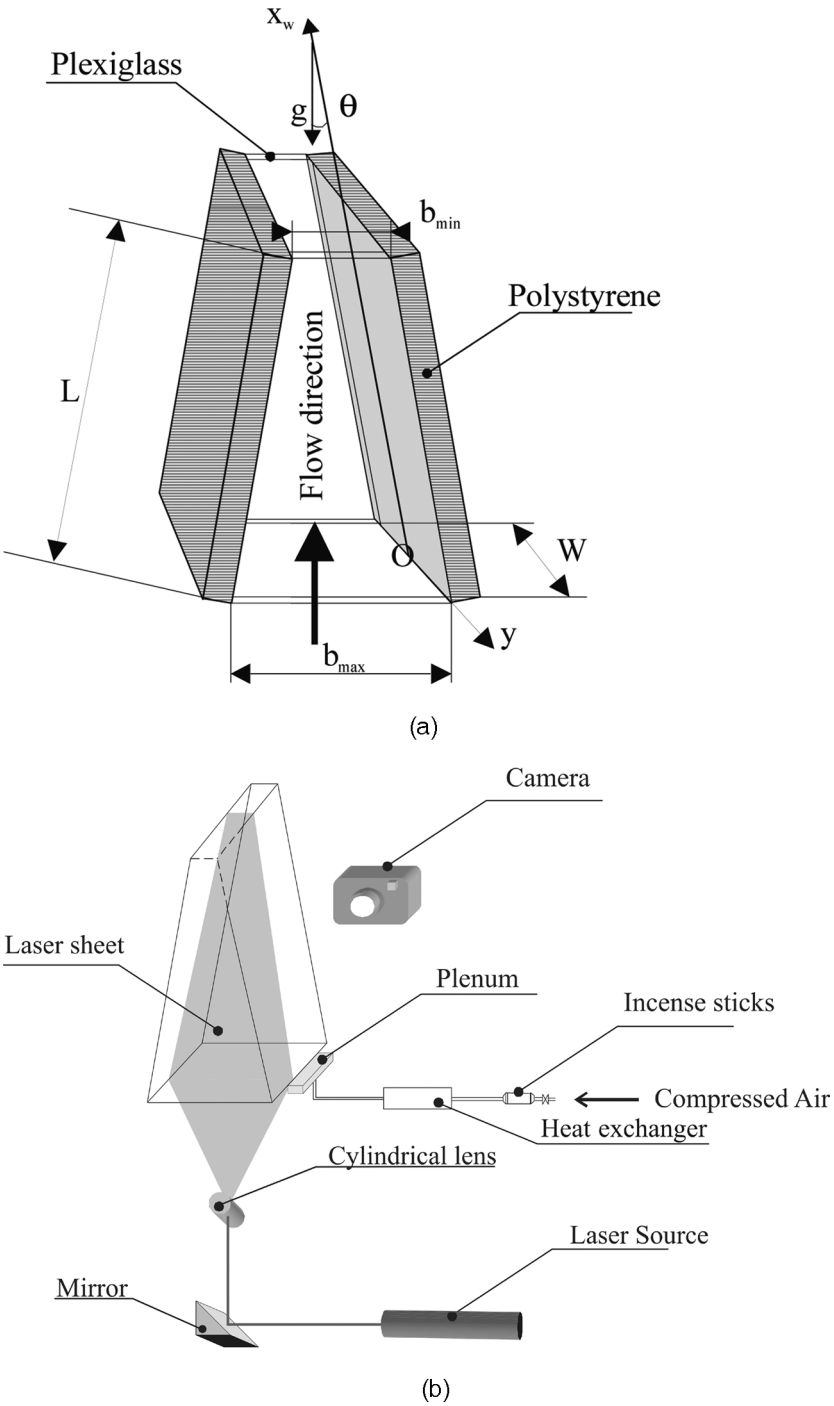

Figure 2. Sketch of the experimental apparatus: (*a*) test section; (*b*) smoke visualization system.

voltages were recorded to 1 μV. Each thermocouple was calibrated in a 0.01 K thermostatic bath using a reference standard thermometer (Pt100). The calibration of the temperature-measuring system showed an estimated precision of the thermocouple–readout system of ±0.2 K. A more detailed description of the experimental apparatus is reported in [12].

Smoke for visualization was generated by burning incense sticks in a steel tube, connected to a compressor (Figure 2*b*). The smoke was injected through a heat exchanger, in order to reduce its temperature, and then it was sent into a plenum. The smoke temperature was measured by means of a thermocouple and was close to the temperature of the ambient air coming into the channel. The smoke was driven to the test section through a small slot situated along the leading edge of the channel. The visualization was made possible by means of a laser sheet, generated by a He–Ne laser source. The laser sheet was produced by placing a mirror near the end of the test section at an angle of 45° with respect to the direction of the main flow, after which a cylindrical lens was placed to enlarge the beam as needed. Fine regulation was allowed by means of a micrometer screw system, in order to obtain photos at the $y = 0$ plane. Pictures of the fluid flow were taken by a Nikon D100 digital camera.

RESULTS AND DISCUSSION

In this article, the analysis is focused on the radiative effects on natural convection in air in a convergent channel uniformly heated at the two principal walls. The wall thickness, t, is 3.2 mm, with the ratio $t/b_{\min}$ varying in the range 0.080–0.46. Its thermal conductivity is 0.198 W/m K, with a solid-to-fluid conductivity ratio $k_s/k_f = 8.18$. The radiation-to-conduction parameter, N_R, varied in the range 0.443–2.54. Results are given for aspect ratios, $L_w/b_{\min}$, ranging from 10 to 58, Rayleigh numbers, $\mathrm{Ra}'^{*}_{b\min}$, ranging from 5.0 to 2.3×10^5, convergent angles, δ, ranging from 0° to 10°, and wall emissivities, ε, ranging from 0.0 to 1.0.

Wall temperature profiles for several wall emissivities, Rayleigh numbers, and convergence angles are reported in Figures 3 and 4. All figures show that wall temperature increases with the distance from the inlet section of the channel. The maximum wall temperature is attained near the outlet of the channel, in accordance with the experimental data presented in [12]. The sudden temperature decrease in the outlet zone is due to the edge effects. The temperature at the channel inlet is not equal to the ambient one, because of the diffusive effects in this zone of the channel.

Figures 3*a* and 3*b*, for $L_w/b_{\min} = 58.0$ and $\delta = 0°$, show that temperature profiles do not depend on ε, except in the exit zone of the channel ($x_w/L_w > 0.85$), where the wall temperatures attain the maximum value and the view factors between the plates and the surroundings are not negligible. As was to be expected, the highest maximum wall temperature is obtained for $\varepsilon = 0.0$, and its value is about 1.68 for $\mathrm{Ra}'^{*}_{b\min} = 20.2$ (Figure 3*a*) and 1.36 for $\mathrm{Ra}'^{*}_{b\min} = 37.0$ (Figure 3*b*). For $\varepsilon = 1.0$ the maximum wall temperature is about 1.67 for $\mathrm{Ra}'^{*}_{b\min} = 20.2$ and 1.32 for $\mathrm{Ra}'^{*}_{b\min} = 37.0$. Increasing $\mathrm{Ra}'^{*}_{b\min}$, the maximum wall temperature is attained at larger x_w/L_w values: for $\varepsilon = 0.0$, x_w/L_w is 0.95 for $\mathrm{Ra}'^{*}_{b\min} = 20.2$ and 0.96 for $\mathrm{Ra}'^{*}_{b\min} = 37.0$. For $\varepsilon = 1.0$, these values are both about 0.94. Figure 3a shows that at $\mathrm{Ra}'^{*}_{b\min} = 20.2$, the difference between the maximum wall temperatures at

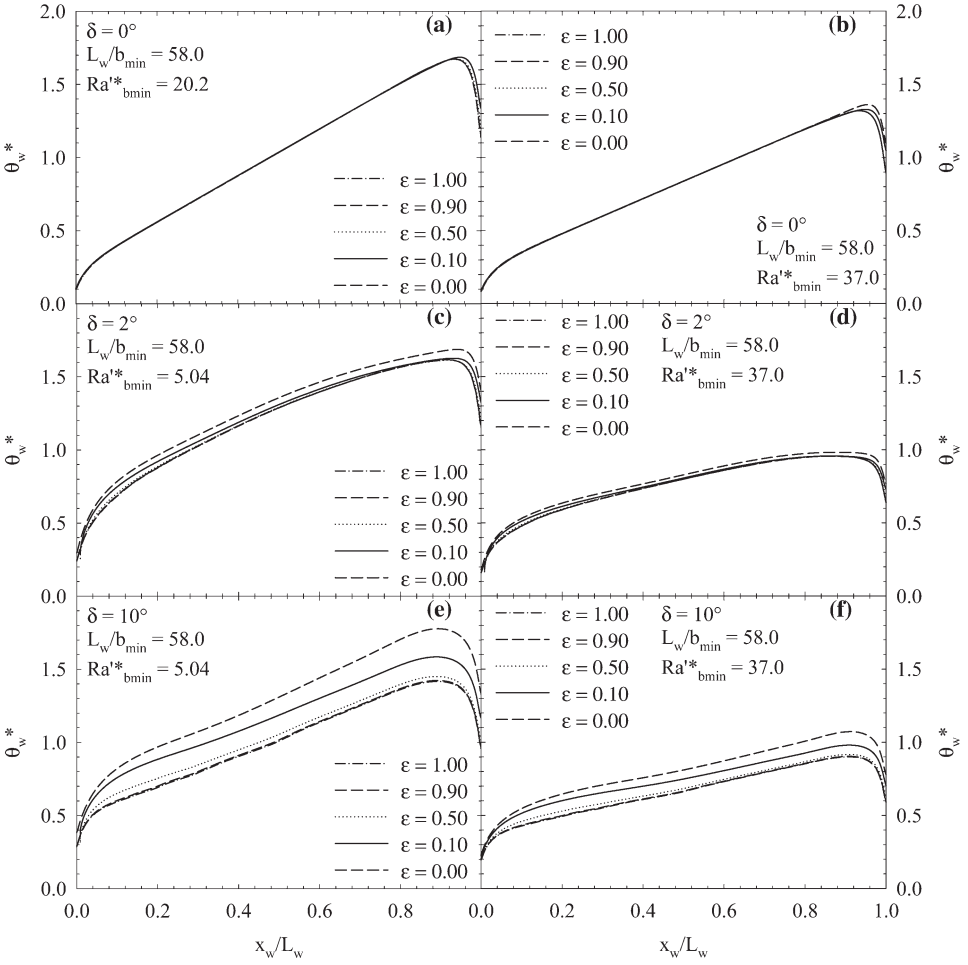

Figure 3. Dimensionless wall temperature profiles versus dimensionless axial coordinate for $L_w/b_{\min} = 58.0$, $t/b_{\min} = 0.46$, $N_R = 0.443$, and for various ε: (*a*) $\delta = 0^\circ$ and $\mathrm{Ra}'^*_{b\min} = 20.2$; (*b*) $\delta = 0^\circ$ and $\mathrm{Ra}'^*_{b\min} = 37.0$; (*c*) $\delta = 2^\circ$ and $\mathrm{Ra}'^*_{b\min} = 5.04$; (*d*) $\delta = 2^\circ$ and $\mathrm{Ra}'^*_{b\min} = 37.0$; (*e*) $\delta = 10^\circ$ and $\mathrm{Ra}'^*_{b\min} = 5.04$; (*f*) $\delta = 10^\circ$ and $\mathrm{Ra}'^*_{b\min} = 37.0$.

$\varepsilon = 0.0$ and at $\varepsilon = 1.0$ is about 0.8% of the maximum wall temperature at $\varepsilon = 0.0$. For $\mathrm{Ra}'^*_{b\min} = 20.2$, Figure 3*a*, the difference between maximum wall temperatures at $\varepsilon = 0.0$ and at $\varepsilon = 1.0$ is about 3.3% of the maximum wall temperature at $\varepsilon = 0.0$ at $x_w/L_w = 0.97$ and about 14.8% in the exit section. Such effect increases at increasing Rayleigh numbers, as can be observed in Figure 3*b* with $\mathrm{Ra}'^*_{b\min} = 37.0$. In fact, the aforementioned differences between maximum wall temperatures at $x_w/L_w = 0.97$ and in the exit section are about 6.2% and 18.6%, respectively.

For both $\mathrm{Ra}'^*_{b\min}$ in Figure 3, the difference between the maximum wall temperature and the wall temperature at the exit section, with respect to the maximum wall temperature, is about 20% for $\varepsilon = 0.0$ and 32% for $\varepsilon = 1.0$. It is interesting to remark that with increasing $\mathrm{Ra}'^*_{b\min}$ the dimensionless wall temperatures decrease, as

is shown in Figure 3. For $Ra'^{*}_{b\min} = 37.0$, maximum dimensionless wall temperature exhibits for $\varepsilon = 0.0$ a 19% decrease with respect to the value at $Ra'^{*}_{b\min} = 20.2$ and 21% for $\varepsilon = 1.0$. It is also important to notice that increasing $Ra'^{*}_{b\min}$ value, for the same $b_{\min}$ value, the dimensional wall temperature increases and the maximum wall temperature increases to about 49% for $\varepsilon = 0.0$ and 45% for $\varepsilon = 1.0$, $Ra'^{*}_{b\min}$ going from 20.2 to 37.0.

Increasing the convergence angle, the differences between the profiles increase, as shown in Figures 3*c*–3*f*. The effect of convergence angle at low values of $Ra'^{*}_{b\min}$ (<40) is pointed out by the results for the lowest value of $b_{\min}$, reported in the following figures. By comparing Figure 3*c* to Figure 3*a*, one can notice that the maximum temperature, for $\varepsilon = 0.0$ ($\theta_{w,\max} = 1.69$), does not depend on $Ra'^{*}_{b\min}$, which is nearly equal to 5.0 in Figure 3*c* and to 20 in Figure 3*a*. For $\varepsilon = 1.0$, the smaller the $Ra'^{*}_{b\min}$, the smaller the dimensionless maximum wall temperature, and its decrease is about 3% when $Ra'^{*}_{b\min}$ increases from 20 to 37. Such a small decrease is due mainly to the increase of the view factor between the channel surfaces and the ambient, which induces a slight decrease in the convective heat transfer. For $Ra'^{*}_{b\min} = 37.0$, the comparison between the values in Figure 3*d* and those in Figure 3*b*, corresponding to the channel with parallel walls ($\delta = 0^{\circ}$), reveals a significant decrease in the dimensionless maximum wall temperature. A nearly 28% decrease both for $\varepsilon = 0.0$ and 1.0 is seen. In all cases, the highest wall temperatures are attained in the lower region of the channel ($x_w/L_w < 0.5$) for $\delta = 2^{\circ}$. In this zone, convective heat transfer is lower because of the lower velocity of the fluid. For example, at $x_w/L_w = 0.2$ and $Ra'^{*}_{b\min} = 37.0$, the increase in the wall temperature with respect to $\delta = 0^{\circ}$ is about 32% for $\varepsilon = 0.0$ and 24% for $\varepsilon = 1.0$.

For $\delta = 2^{\circ}$, increasing ε decreases wall temperatures at all points. For $Ra'^{*} = 5.04$, Figure 3*d*, going from $\varepsilon = 0.0$ to $\varepsilon = 0.1$, the wall temperature decrease is about 4.5% at $x_w/L_w = 0.2$ and 5.7% at the exit section, $x_w/L_w = 1.0$. For $\varepsilon = 1.0$, these values are about 9% at $x_w/L_w = 0.2$, and 19% at $x_w/L_w = 1.0$. The dimensionless maximum wall temperature decrease in going from $\varepsilon = 0.0$ to $\varepsilon = 1.0$ is about 4.1%. It is interesting to observe that in the range $0.7 < x_w/L_w < 0.92$, wall temperature profiles for $\varepsilon = 0.1$ and $\varepsilon = 1.0$ are very close. A similar trend is also observed in Figure 3*d*, for $\varepsilon = 0.1$ and $Ra'^{*}_{b\min} = 37.0$.

For all ε values, a significant decrease in the dimensionless wall temperature is exhibited, going from $Ra'^{*} = 5.04$, Figure 3*c*, to $Ra'^{*}_{b\min} = 37.0$, Figure 3*d*. In particular, the decrease in dimensionless maximum wall temperature is about 42% for $\varepsilon = 0.0$ and 41% for $\varepsilon = 1.0$. Figure 3*d*, for $Ra'^{*}_{b\min} = 37.0$, shows a less marked effect of increasing ε on wall temperature decrease than that exhibited in Figure 3*c*, for $Ra'^{*}_{b\min} = 5.04$. Going from $\varepsilon = 0.0$ to $\varepsilon = 1.0$, the temperature decrease is about 7.2% at $x_w/L_w = 0.2$, and 17% at the channel outlet, whereas the decrease in maximum wall temperature is about 2.5%.

Figures 3*e* and 3*f*, for $Ra'^{*}_{b\min} = 5.04$ and $Ra'^{*}_{b\min} = 37.0$, show that for $\varepsilon = 0.0$, dimensionless maximum wall temperature at $\delta = 10^{\circ}$ is higher than at $\delta = 2^{\circ}$ (Figures 3*c* and 3*d*), as was also reported in [13]. On the other hand, for $\varepsilon = 0.10$ and $Ra'^{*}_{b\min} = 5.04$, Figure 3*e* shows that it decreases, whereas for $Ra'^{*}_{b\min} = 37.0$ (Figure 3*f*) it is still slightly higher. This indicates that, for a given $b_{\min}$ value, the optimal convergence angle in terms of minimum value of the maximum wall temperature depends on ε and $Ra'^{*}_{b\min}$. For $Ra'^{*}_{b\min} = 5.04$, Figure 3*e*, the increase in

dimensionless maximum wall temperature in going from $\delta = 2^\circ$ to $\delta = 10^\circ$ is about 5.6% at $\varepsilon = 0.0$ and the decreases are about 2.7% and 12.6% at $\varepsilon = 0.1$ and $\varepsilon = 1.0$, respectively. For $Ra'^{*}_{b\min} = 37.0$, Figure 3*f*, going from $\delta = 2^\circ$ to $\delta = 10^\circ$, the variations in dimensionless maximum wall temperature are about 9.0% for $\varepsilon = 0.0$, 2.3% for $\varepsilon = 0.1$, and -6.0% for $\varepsilon = 1.0$.

For the same $b_{\min}$ value and $Ra'^{*}_{b\min}$, increasing the channel convergence increases the difference between wall temperature profiles, as observed in Figures 3*e* and 3*f*. Moreover, the difference between profiles is higher at lower $Ra'^{*}_{b\min}$ values. For $Ra'^{*}_{b\min} = 5.04$, Figure 3*e*, at $x_w/L_w = 0.2$, going from $\varepsilon = 0.0$ to $\varepsilon = 0.1$, the decrease is about 8%, and it is about 29% when varying ε from 0.0 to 1.0. Increasing ε from 0.0 to 0.1 decreases the dimensionless maximum wall temperature by about 11% and increasing ε from 0.0 to 1.0 decreases it by about 20%. For $Ra'^{*}_{b\min} = 37.0$, Figure 3*f*, at $x_w/L_w = 0.2$ these values are about 7% and 24%, whereas the variations in the maximum temperature are about 8% and 16%, respectively. The decrease of dimensionless maximum wall temperature in going from $Ra'^{*}_{b\min} = 5.04$ to 37.0 is about 40% for $\varepsilon = 0.0$, 38% for $\varepsilon = 0.1$, and 36% for $\varepsilon = 1.0$.

The dimensionless wall temperature decreases considerably at decreasing aspect ratios, $L_w/b_{\min}$, which in the present analysis means a larger minimum channel gap, $b_{\min}$.

Interesting considerations can be made by comparing Figures 3*c*–3*d* to Figures 4*a*–4*b*, for $\delta = 2^\circ$, and Figures 3*e*–3*f* to Figures 4*c*–4*d*, for $\delta = 10^\circ$. For

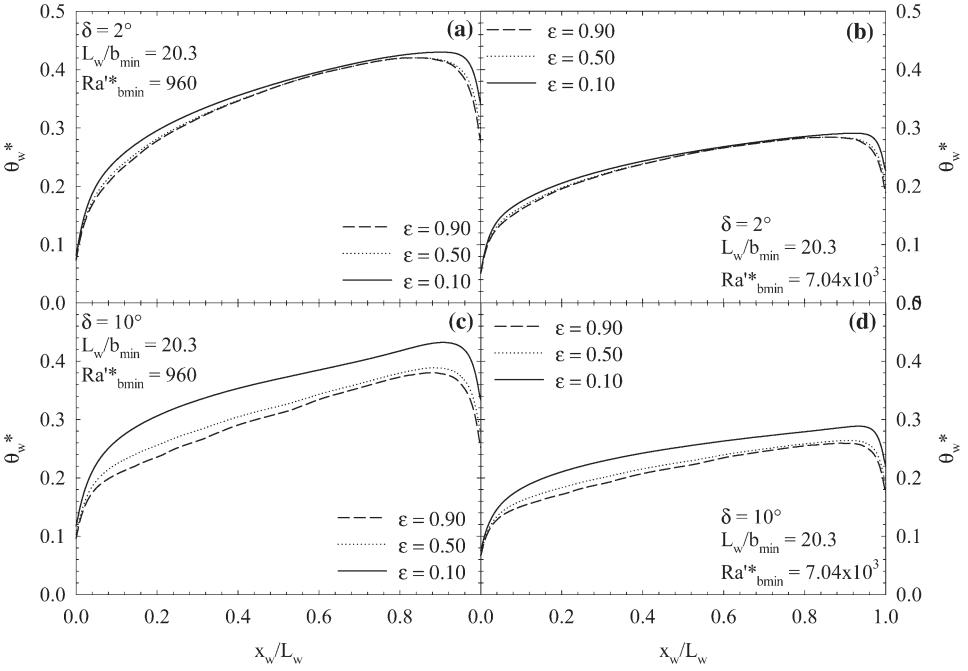

Figure 4. Dimensionless wall temperature profiles versus dimensionless axial coordinate for $L_w/b_{\min} = 20.3$, $t/b_{\min} = 0.16$, $N_R = 1.27$, and for various ε: (*a*) $\delta = 2^\circ$ and $Ra'^{*}_{b\min} = 960$; (*b*) $\delta = 2^\circ$ and $Ra'^{*}_{b\min} = 7.04 \times 10^3$; (*c*) $\delta = 10^\circ$ and $Ra'^{*}_{b\min} = 960$; (*d*) $\delta = 10^\circ$ and $Ra'^{*}_{b\min} = 7.04 \times 10^3$.

$\delta = 2^\circ$ the ratio of dimensionless maximum wall temperatures in Figure 4*a* ($L_w/b_{\min} = 20.3$ and $\mathrm{Ra}'^*_{b\min} = 960$) to those in Figure 3*c* ($L_w/b_{\min} = 58.0$ and $\mathrm{Ra}'^*_{b\min} = 5.04$) is nearly 0.26 for $\varepsilon = 0.1$ and 0.9. In dimensional terms, at the same wall heat flux value, the aforementioned ratio is about 0.75 for $\varepsilon = 0.1$ and 0.9, that is, a 25% lower maximum wall temperature rise. The same ratio of the value in Figure 4*b* ($\mathrm{Ra}'^*_{b\min} = 7.04 \times 10^3$) to that in Figure 3*d* ($\mathrm{Ra}'^*_{b\min} = 37.0$) is about 0.30 for $\varepsilon = 0.1$ and 0.9, whereas in dimensional terms it is about 0.85 for both ε values, giving a 15% reduction in maximum wall temperature rise. For $\delta = 10^\circ$ the ratios of values in Figure 4*c* to those in Figure 3*e* are about 0.27 and 0.77, whereas those of values in Figure 4*d* to those in Figure 3*f* are 0.29 for dimensionless values, and 0.84 for dimensional temperature rise.

In Figure 4, for $\delta = 2^\circ$ and $L_w/b_{\min} = 20.3$, one can notice that increasing $\mathrm{Ra}'^*_{b\min}$ from 960 (Figure 4*a*) to 7.04×10^3 (Figure 4*b*), the dimensionless wall temperature decreases and its maximum value exhibits a nearly 32% decrease for $\varepsilon = 0.1$ and 0.9. Figure 4*a* also shows a 2.3% decrease in the dimensionless maximum wall temperature when ε goes from 0.1 to 0.9, whereas for $\mathrm{Ra}'^*_{b\min} = 7.04 \times 10^3$ the decrease is about 3.5%. Increasing the convergence angle δ up to 10°, Figures 4*c*–4*d*, practically does not affect wall temperature. In fact, for $\varepsilon = 0.10$ the maximum difference between dimensionless wall temperatures at $\delta = 10^\circ$ and at $\delta = 2^\circ$ is about 1%, reference being made to the temperature at $\delta = 2^\circ$. For $\mathrm{Ra}'^*_{b\min} = 960$, Figures 4*a* and 4*c* show that differences in wall temperature profiles both at $\varepsilon = 0.50$ and at $\varepsilon = 0.90$ are nearly 7% and 9%, respectively, whereas in Figures 4*b* and 4*d*, for $\mathrm{Ra}'^*_{b\min} = 7.04 \times 10^3$, their values are about 6% and 8%.

The stream-function fields for various values of $L_w/b_{\min}$, δ, and $\mathrm{Ra}'^*_{b\min}$ are presented in Figure 5. In Figures 5*a*–5*d*, $L_w/b_{\min} = 58.0$, one can remark that for all convergence angles the thermal plume leaving the channel drags the fluid from the ambient. For $\delta = 0^\circ$ and $\delta = 2^\circ$, streamlines are parallel to the walls and the motion is practically fully developed. In fact, it was observed, but not presented here, that for $\delta = 0^\circ$ the velocity profiles at half-channel height and at the channel outlet are very similar, whereas for $\delta = 2^\circ$ the flow is developed in the second half of the channel. By increasing convergence angles, a recirculating region, with two symmetrical vortices, is detected in the channel. For $\delta = 5^\circ$, Figure 5*c*, the recirculating region is located in the central part of the channel. For $\delta = 10^\circ$, Figure 5*d*, the two symmetrical vortices are wider. The recirculation is determined by the interaction of the two symmetrical boundary layers in the outlet region of the channel. For large values of $L_w/b_{\min}$, a strong interaction between the two boundary layers occurs and the flow chokes in the channel, because of the boundary-layer thickness, the $L_w/b_{\min}$ value, and the fluid velocity. Comparing Figures 5*a* and 5*d*, $\mathrm{Ra}'^*_{b\min} = 5.04$, to Figures 5*e* and 5*f*, $\mathrm{Ra}'^*_{b\min} = 37.0$, we can remark that when the Rayleigh number increases, the recirculating region shifts toward the channel outlet, because of the reduction in the thickness of the boundary layer. In fact, the ratio of the boundary-layer thickness to the channel spacing decreases as $\mathrm{Ra}'^*_{b\min}$ increases. For a larger channel spacing ($L_w/b_{\min} = 12.6$), Figures 5*g* and 5*h*, the interaction between the boundary layers along the two heated walls at the channel outlet decreases significantly and no recirculating region occurs for all the considered convergence angles. In the inlet region of the channel the *vena contracta* phenomenon is observed, and for an assigned $L_w/b_{\min}$ it is more marked at increasing δ and Ra'^*. Increasing the aspect

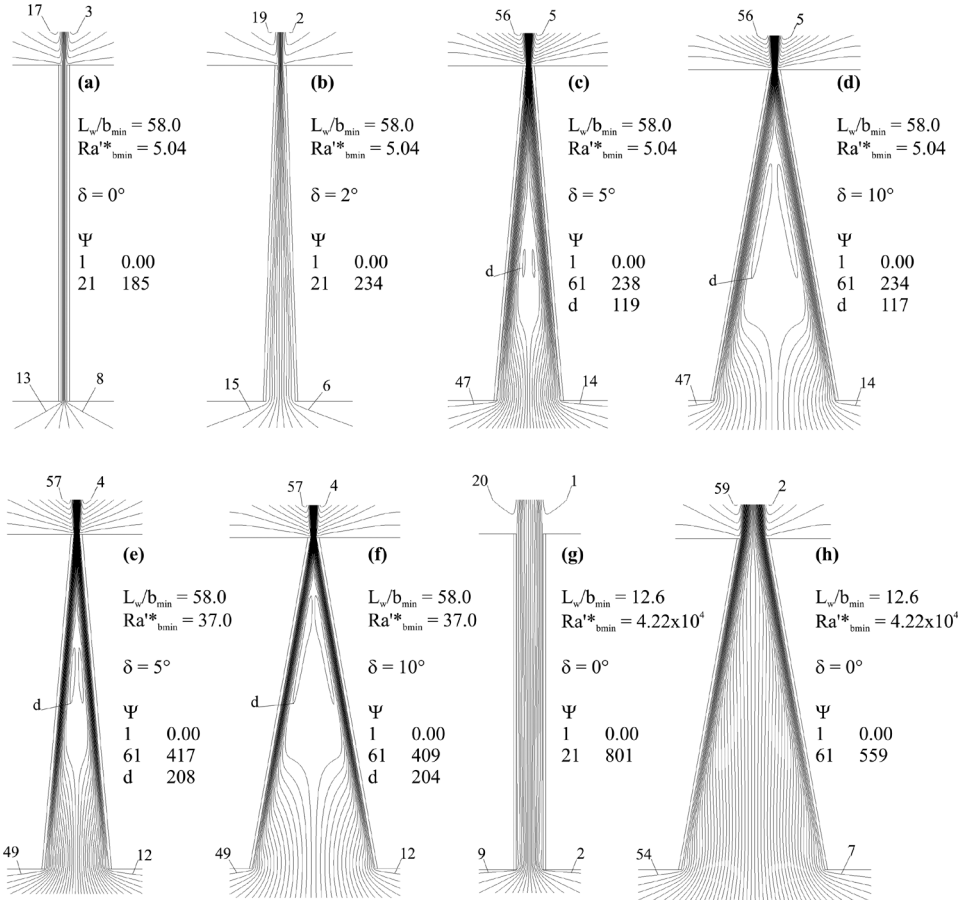

Figure 5. Stream lines: (*a*) $L_w/b_{\min} = 58.0$, $\mathrm{Ra}'^*_{b\min} = 5.04$, $\delta = 0^\circ$; (*b*) $L_w/b_{\min} = 58.0$, $\mathrm{Ra}'^*_{b\min} = 5.04$, $\delta = 2^\circ$; (*c*) $L_w/b_{\min} = 58.0$, $\mathrm{Ra}'^*_{b\min} = 5.04$, $\delta = 5^\circ$; (*d*) $L_w/b_{\min} = 58.0$, $\mathrm{Ra}'^*_{b\min} = 5.04$, $\delta = 10^\circ$; (*e*) $L_w/b_{\min} = 58.0$, $\mathrm{Ra}'^*_{b\min} = 37.0$, $\delta = 5^\circ$; (*f*) $L_w/b_{\min} = 58.0$, $\mathrm{Ra}'^*_{b\min} = 37.0$, $\delta = 10^\circ$; (*g*) $L_w/b_{\min} = 12.6$, $\mathrm{Ra}'^*_{b\min} = 4.22 \times 10^4$, $\delta = 0^\circ$; (*h*) $L_w/b_{\min} = 12.6$, $\mathrm{Ra}'^*_{b\min} = 4.22 \times 10^4$, $\delta = 10^\circ$.

ratio, $L_w/b_{\min}$, this effect increases and the *vena contracta* moves toward the upper region of the channel.

In Figure 6 the temperature contours, for $L_w/b_{\min} = 58.0$ and $\delta = 5^\circ$ and 10°, are presented for $\mathrm{Ra}'^*_{b\min} = 5.04$ and 37.0. It is observed that increasing the convergence angle δ, the central zone in the channel at ambient temperature increases. The recirculation zone is exhibited by contour shapes in the central zone of the channel, Figures 6*a* and 6*b*. Moreover, it is observed that for the larger $\mathrm{Ra}'^*_{b\min}$, Figures 6*c* and 6*d*, the isotherms confirm the position of the two vortices in the upper part of the channel. A typical shape of the isotherm contours for the fluid flow without recirculation zone is exhibited in Figures 6*e* and 6*f*.

Some pictures of flow visualization are reported in Figure 7. Pictures for different $L_w/b_{\min}$, $\mathrm{Ra}'^*_{b\min}$, and δ values are presented in Figures 7*a*–7*g*. For $L_w/b_{\min} = 58.0$, $\mathrm{Ra}'^*_{b\min} = 5.04$, and for small convergence angles ($\delta = 2^\circ$),

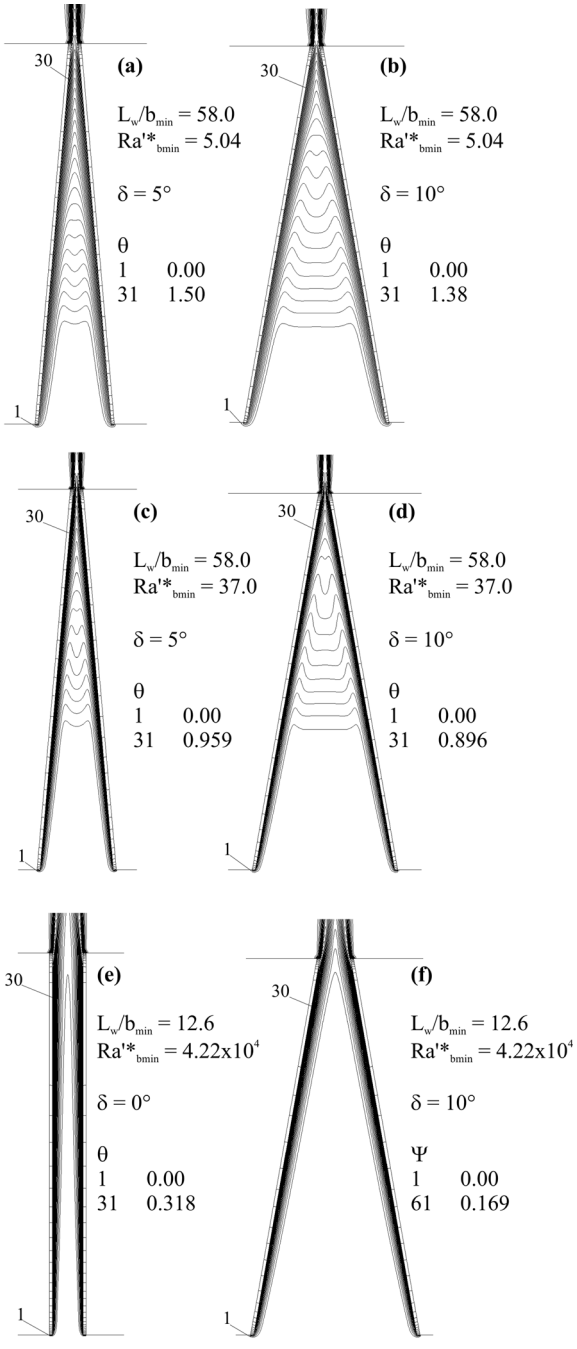

Figure 6. Air temperature fields: (*a*) $L_w/b_{\min} = 58.0$, $\mathrm{Ra}'^*_{b\min} = 5.04$, $\delta = 5^\circ$; (*b*) $L_w/b_{\min} = 58.0$, $\mathrm{Ra}'^*_{b\min} = 5.04$, $\delta = 10^\circ$; (*c*) $L_w/b_{\min} = 58.0$, $\mathrm{Ra}'^*_{b\min} = 37.0$, $\delta = 5^\circ$; (*d*) $L_w/b_{\min} = 58.0$, $\mathrm{Ra}'^*_{b\min} = 37.0$, $\delta = 10^\circ$; (*e*) $L_w/b_{\min} = 12.6$, $\mathrm{Ra}'^*_{b\min} = 4.22 \times 10^4$, $\delta = 0^\circ$; (*f*) $L_w/b_{\min} = 12.6$, $\mathrm{Ra}'^*_{b\min} = 4.22 \times 10^4$, $\delta = 10^\circ$.

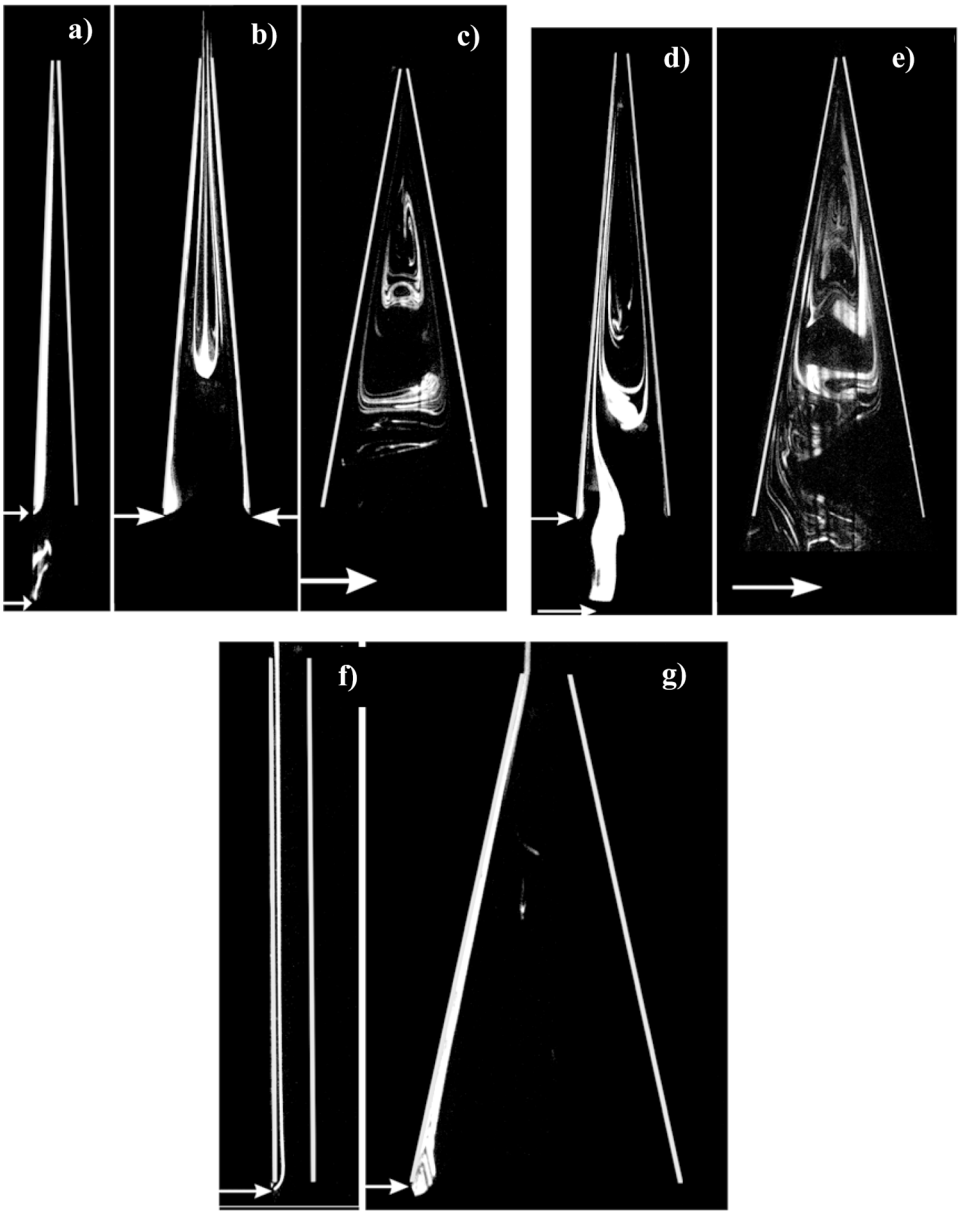

Figure 7. Flow visualization: (*a*) $L_w/b_{\min} = 58.0$, $\mathrm{Ra}'^{*}_{b\min} = 5.04$, $\delta = 2^{\circ}$; (*b*) $L_w/b_{\min} = 58.0$, $\mathrm{Ra}'^{*}_{b\min} = 5.04$, $\delta = 5^{\circ}$; (*c*) $L_w/b_{\min} = 58.0$, $\mathrm{Ra}'^{*}_{b\min} = 5.04$, $\delta = 10^{\circ}$; (*d*) $L_w/b_{\min} = 58.0$, $\mathrm{Ra}'^{*}_{b\min} = 37.0$, $\delta = 5^{\circ}$; (*e*) $L_w/b_{\min} = 58.0$, $\mathrm{Ra}'^{*}_{b\min} = 5.04$, $\delta = 10^{\circ}$; (*f*) $L_w/b_{\min} = 12.6$, $\mathrm{Ra}'^{*}_{b\min} = 4.22 \times 10^4$, $\delta = 0^{\circ}$; (*g*) $L_w/b_{\min} = 12.6$, $\mathrm{Ra}'^{*}_{b\min} = 4.22 \times 10^4$, $\delta = 10^{\circ}$.

Figure 7*a*, the photographs show that the flow is laminar and the smoke moves along the wall in the channel. Increasing the convergence angle, $\delta = 5^{\circ}$, Figure 7*b* shows a part of the smoke adjacent to the wall and a two-cell recirculating region in the

central part of the channel. This is in accordance with numerical results presented in Figure 5*c*. For $\delta = 10^\circ$, Figure 7*c* exhibits a large stagnation region and a larger recirculating region, in good agreement with numerical results presented in Figure 5*d*. At larger Rayleigh number, for $\delta = 5^\circ$, Figure 7*d*, the recirculating region is less extended and it moves toward the channel outlet zone, as was shown in the numerical results presented in Figure 5*e*. The same considerations can be made by observing Figure 7*e* for $\delta = 10^\circ$. Figures 7*f* and 7*g* confirm that in the largest channel there is no recirculation region.

Convective Nusselt number, Nu, as well as convective and radiative Nusselt number, Nu*, have been correlated to the corresponding Rayleigh numbers, Ra′ and Ra′*. The following equations are obtained:

$$\mathrm{Nu}_{b\min} = 0.55\,\mathrm{Ra}'^{0.22}_{b\min} \tag{14}$$

with $r^2 = 0.991$, in the $4.4 \le \mathrm{Ra}'_{b\min} \le 1.5 \times 10^5$, $10 \le L_w/b_{\min} \le 58$, and $0^\circ \le \delta \le 10^\circ$ ranges;

$$\mathrm{Nu}_{b\max} = 0.57\,\mathrm{Ra}'^{0.21}_{b\max} \tag{15}$$

with $r^2 = 0.990$, in the $4.4 \le \mathrm{Ra}'_{b\max} \le 2.9 \times 10^8$, $10 \le L_w/b_{\min} \le 58$, and $0^\circ \le \delta \le 10^\circ$ ranges.

Numerical data and correlations are presented in Figures 8*a*–8*b*. The regression coefficient is slightly larger when $b_{\min}$ is chosen as the characteristic length. For small Rayleigh numbers, more significant differences between numerical predictions and correlations are observed, for $b = b_{\min}$ and $\delta = 0^\circ$ and, therefore, the correlation with the dimensionless numbers referred to $b_{\max}$ is recommended in this case, mostly for $5 < \mathrm{Ra}'_{b\min} < 30$.

If the radiative heat flux is accounted for, larger deviations between numerical data and the correlation equation for the dimensionless parameters referred to $b_{\min}$ are exhibited. Therefore, only a correlation where Nusselt and Rayleigh numbers are referred to $b_{\max}$ is proposed:

$$\mathrm{Nu}^*_{b\max} = 0.54\,\mathrm{Ra}'^{*0.22}_{b\max} \tag{16}$$

with $r^2 = 0.992$ in the $5.0 \le \mathrm{Ra}'^*_{b\max} \le 4.3 \times 10^8$, $10 \le L_w/b_{\min} \le 58$, and $0^\circ \le \delta \le 10^\circ$ ranges. In Figure 8*c*, numerical data and the correlation equation (16) are reported for the previously cited process parameters.

For the sake of comparison, monomial correlations by experimental data given in [12] are presented in the following:

$$\mathrm{Nu}_{b\min} = 0.58\,\mathrm{Ra}'^{0.22}_{b\min} \tag{17}$$

$$\mathrm{Nu}_{b\max} = 0.58\,\mathrm{Ra}'^{0.21}_{b\max} \tag{18}$$

$$\mathrm{Nu}^*_{b\max} = 0.56\,\mathrm{Ra}'^{*0.22}_{b\max} \tag{19}$$

and reported in Figure 8. The agreement between the coefficients of the proposed correlations is very good.

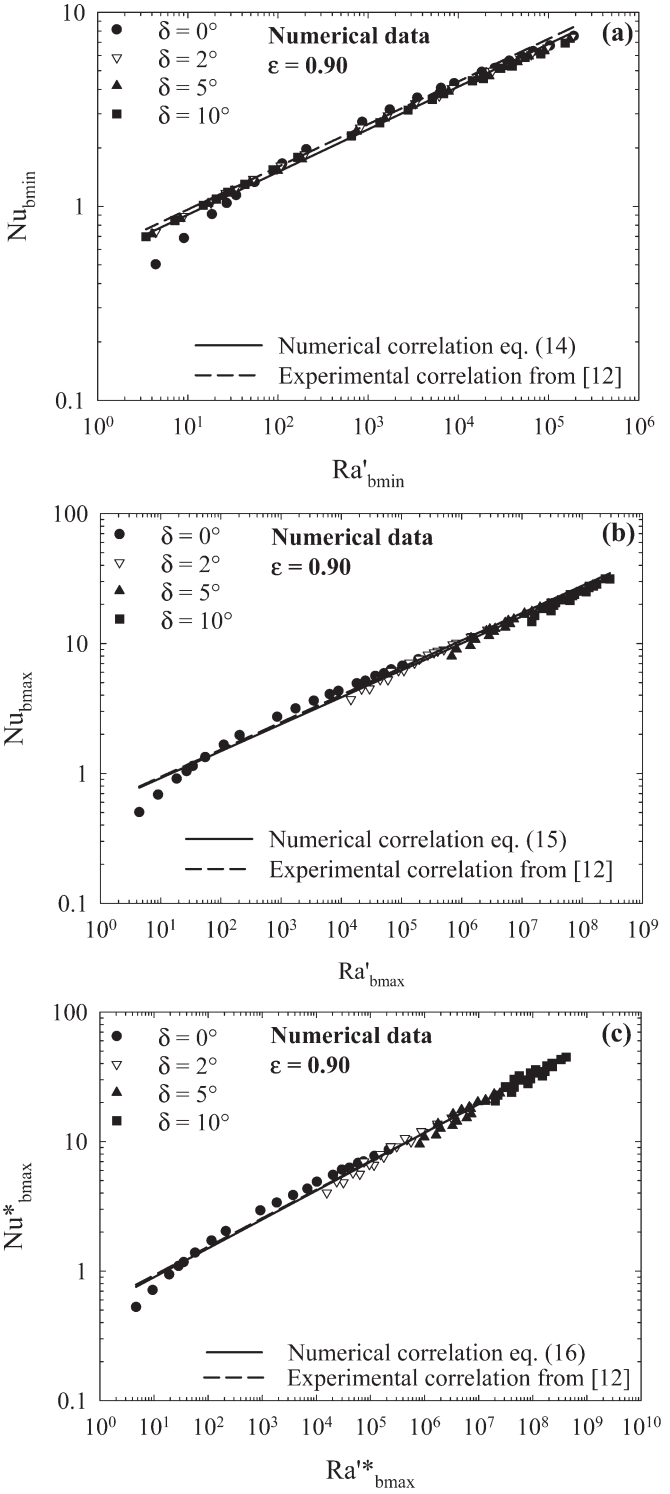

Figure 8. Nusselt numbers versus Rayleigh numbers for $\varepsilon = 0.90$ and for various δ.

CONCLUSIONS

A numerical investigation on natural convection in air in a convergent channel, with two principal flat plates at uniform heat flux, was carried out. Heat conduction in the walls and the effects of the walls emissivity were taken into account. Laminar two-dimensional steady-state conditions were assumed. An extended computational domain was adopted in order to take into account the diffusion by both momentum and energy outside the channel. Results in terms of wall dimensionless temperature profiles as a function of the wall inclination angle, the interval spacing, and the heat flux were given for various values of wall emissivity.

Wall temperature profiles showed that, at any convergence angle, increasing the Rayleigh number decreases the difference between maximum wall temperatures at various wall emissivities. Radiation effect was more significant at low Rayleigh numbers ($Ra'^{*}_{b\min} < 40$). As was expected, in vertical symmetrically heated channels, the larger the convergence angle, the larger the radiative heat transfer. For larger aspect ratio, $L_w/b_{\min} \sim 60$, high maximum wall temperature decreases were exhibited at low Rayleigh numbers, going from $\delta = 0^\circ$ to $\delta = 2^\circ$. At larger Rayleigh numbers, larger variations in maximum wall temperatures were observed by increasing the convergence angle from 5° to 10°.

Stream-function and air temperature fields for low Rayleigh numbers and large aspect ratios showed similar flow patterns for $\delta = 0^\circ$ and 2°, whereas for $\delta \geq 5^\circ$ a recirculating region with two symmetrical vortices was exhibited in the upper part of the channel. The recirculating region turned out to be larger for larger converging angles and Rayleigh numbers. For low aspect ratios and large channel spacings, no recirculating region was detected at all convergence angles considered. Pictures from flow visualization were in very good agreement with numerical predictions at both low and high Rayleigh numbers.

Simple monomial correlation equations for convective as well as for convective and radiative Nusselt numbers in terms of Rayleigh numbers were derived in the $4.4 < Ra'_{b\min} < 1.5 \times 10^5$, $5.0 < Ra'^{*}_{b\max} < 4.3 \times 10^8$, $10 \leq L_w/b_{\min} \leq 58$, and $0^\circ \leq \delta \leq 10^\circ$ ranges. The best regression coefficient was obtained by using the maximum channel gap as the characteristic length. The agreement between experimental and numerical correlations was very good.

REFERENCES

1. F. P. Incropera, *Liquid Cooling of Electronic Devices by Single-Phase Convection*, Wiley, New York, 1999.
2. O. Manca, B. Morrone, S. Nardini, and V. Naso, Natural Convection in Open Channels, in B. Sundén and G. Comini (eds.), *Computational Analysis of Convection Heat Transfer*, chap. 7, pp. 235–278, WIT Press, Southampton, UK, 2000.
3. G. D. Raithby and K. G. T. Hollands, Natural Convection, in W. M. Rohsenow, J. P. Hartnett, and Y. I. Cho (eds.), *Handbook of Heat Transfer*, chap. 7, pp. 4.1–4.99, McGraw-Hill, New York, 1998.
4. A. Bejan, *Shape and Structure, from Engineering to Nature*, Cambridge University Press, Cambridge, UK, 2000.
5. G. A. Ledezma and A. Bejan, Optimal Geometric Arrangement of Staggered Vertical Plates in Natural Convection, *J. Heat Transfer*, vol. 119, pp. 700–708, 1997.

6. E. M. Sparrow, R. Ruiz, and L. F. A. Azevedo, Experiments and Numerical Investigation of Natural Convection in Convergent Vertical Channels, *Int. J. Heat Mass Transfer*, vol. 31, pp. 907–915, 1988.
7. K. D. Kihm, J. H. Kim, and L. Fletcher, Investigation of Natural Convection Heat Transfer in Vertical Converging Channel Flows Using a Specklegram Technique, *J. Heat Transfer*, vol. 115, pp. 140–148, 1993.
8. S. A. Said, Investigation of Natural Convection in Convergent Vertical Channels, *Int. J. Energy Res.*, vol. 20, pp. 559–567, 1996.
9. J. S. Shalash, J. D. Tarasuk, and D. Naylor, Experimental and Numerical Studies of Natural Convection Heat Transfer in Vertical Converging Channel Flows, *Proc. 4th Experimental Heat Transfer, Fluid Mechanics and Thermodynamics Conf.*, Brussels, June 2–6 1997, vol. 4, pp. 2167–2174.
10. A. S. Kaiser, B. Zamora, and A. Viedma, Correlations for Nusselt Number in Natural Convection in Vertical Converging Channels at Uniform Wall Temperature by Numerical Investigation, *Int. J. Heat Fluid Flow*, vol. 25, pp. 671–682, 2004.
11. A. Bejan, A. K. da Silva, and S. Lorente, Maximal Heat Transfer Density in Vertical Morphing Channels with Natural Convection, *Numer. Heat Transfer A*, vol. 45, pp. 135–152, 2004.
12. N. Bianco, O. Manca, S. Nardini, and V. Naso, An Experimental Study of Radiative Effects on Natural Convection in Air in Convergent Channels, Paper IMECE2003-41269, *Proc. ASME–IMECE,* Washington, DC, November 15–21, 2003.
13. N. Bianco and S. Nardini, Numerical Analysis of Natural Convection in Air in a Vertical Convergent Channel with Uniformly Heated Conductive Walls, *Int. Commun. Heat Mass Transfer*, vol. 32, pp. 758–769, 2005.
14. A. A. Dehghan and M. Behnia, Combined Natural Convection-Conduction and Radiation Heat Transfer in a Discretely Heated Open Cavity, *J. Heat Transfer*, vol. 118, pp. 56–64, 1996.
15. J. R. Carpenter, D. G. Briggs, and V. Sernas, Combined Radiation and Developing Laminar Free Convection between Vertical Flat Plates with Asymmetric Heating, *J. Heat Transfer*, vol. 98, pp. 95–100, 1976.
16. O. Manca and V. Naso, Experimental Analysis of Natural Convection and Thermal Radiation in Vertical Channels, *ASME HTD*, vol. 145, pp. 13–21, 1990.
17. A. Moutsoglou, J. H. Rhee, and J. K. Won, Natural Convection-Radiation Cooling of a Vented Channel, *Int. J. Heat Mass Transfer*, vol. 35, pp. 2855–2863, 1992.
18. S. B. Sathe and B. G. Sammakia, A Numerical Study of the Thermal Performance of a Tape Ball Grid Array (TBGA) Package, *J. Electronic Packaging*, vol. 122, pp. 107–114, 2000.
19. A. Campo, O. Manca, and B. Morrone, Numerical Analysis of Partially Heated Vertical Parallel Plates in Natural Convective Cooling, *Numer. Heat Transfer A*, vol. 36, pp. 129–151, 1999.
20. B. Gebhart, Y. Jaluria, R. Mahajan, and B. Sammakia, *Buoyancy-Induced Flows and Transport*, Hemisphere, Washington, DC, 1988.
21. J. L. Lage, J. S. Lim, and A. Bejan, Natural Convection with Radiation in Cavity with Open Top End, *J. Heat Transfer*, vol. 114, pp. 479–486, 1992.
22. Fluent Incorporated, *Fluent 6.1, User Manual*, Lebanon, New Hampshire, 2003.
23. P. J. Coelho and M. G. Carvalho, A Conservative Formulation of the Discrete Transfer Method, *J. Heat Transfer*, vol. 119, pp. 118–128, 1997.
24. J. P. Roache, *Verification and Validation in Computational Science and Engineering*, Hermosa, Albuquerque, NM, 1998.